Fracture characterization using frequency-dependent shear wave anisotropy analysis of microseismic data

Geophysical Journal International

Geophys. J. Int. (2011) **185,** 1059–1070 doi: 10.1111/j.1365-246X.2011.04997.x

Fracture characterization using frequency-dependent shear wave anisotropy analysis of microseismic data

O. H. Al-Harrasi,[1,2] J.-M. Kendall[1] and M. Chapman[3]

[1] *Department of Earth Sciences, Wills Memorial Building, University of Bristol, Bristol,* BS8 1RJ, *UK*
E-mail: o.alharrasi@gmail.com
[2] *Petroleum Development Oman,* P. Box 81, P.C. 100, *Muscat, Sultanate of Oman*
[3] *Grant Institute, The King's Buildings, West Mains Road, University of Edinburgh, Edinburgh, EH9 JW, UK*

Accepted 2011 February 23. Received 2011 February 23; in original form 2010 August 28

SUMMARY

The presence of fractures in hydrocarbon reservoirs can enhance porosity and permeability, and consequently increase production. The use of seismic anisotropy to characterize fracture systems has gained much interest in the last two decades. However, estimating fracture sizes from observations of seismic anisotropy has not been possible. Recent work has shown that frequency-dependent anisotropy (FDA) is very sensitive to the length-scale of the causative mechanism for the anisotropy. In this study, we observe FDA in a microseismic data set acquired from a carbonate gas field in Oman. The frequency-dependent shear wave anisotropy observations are modelled using a poroelastic model, which considers fluid communication between grain size pore spaces and larger scale fractures. A grid search is performed over fracture parameters (radius, density and strike) to find the model that best fits the real data. The results show that fracture size varies from the microscale within the shale cap rocks, to the metre-scale within the gas reservoir, to the centimetre-scale within the non-producing part of the carbonate formation. The lateral variation in fracture density agrees with previous conclusions from ordinary shear wave splitting (SWS) analysis. Cumulatively, the results show the potential for characterizing fracture systems using observations of FDA.

Key words: Downhole methods; Fracture and flow; Seismic anisotropy.

1 INTRODUCTION

Fractures in sedimentary settings play a crucial role in hydrocarbon production as they enhance porosity and permeability. Thus, fracture orientations, densities and sizes are of interest to reservoir engineers. Much of our knowledge about fractures comes from exploration seismology, specifically through the study of fracture-induced shear wave splitting (SWS). In SWS analysis, fracture orientations are inferred from the polarization of the fast shear wave (Φ), whereas fracture density is estimated from the anisotropy magnitude (the delay time between the fast and slow shear waves (δt)). However, with such analysis, it is unknown whether the anisotropy is due to microscale cracks or macroscale fractures. Reservoir engineers therefore do not generally use observations of seismic anisotropy as a routine method of fracture characterization. Quantitative discrimination between the two scales (micro and macro) when characterizing fractures is important because the latter controls reservoir storability and fluid flow.

Several studies have recently reported the dependence of anisotropy on frequency. Marson-Pidgeon & Savage (1997) observed evidence of frequency-dependent anisotropy (FDA) in earthquake data recorded in New Zealand using SKS and ScS phases. Rumpker *et al.* (1999) demonstrated the frequency-dependent nature of splitting parameters from such seismic phases in layered anisotropic media. Similar observations were shown by Chesnokov *et al.* (2001), Liu *et al.* (2003) and Maultzsch *et al.* (2003) using multicomponent VSP data and by Al-Anboori *et al.* (2006) using microseismic data. These observations were based on SWS analysis. Carter & Kendall (2006) observed frequency-dependent attenuation anisotropy in microseismic data acquired from the Valhal oilfield, North Sea. Seismic attenuation anisotropy was examined by comparing the relative frequency content of the fast and slow split shear waves.

The two most likely mechanisms that can cause velocity dispersion and consequently FDA are scattering by inhomogenities and fluid flow in fractured porous rocks (Liu *et al.* 2003). Anisotropy induced by scattering occurs only when the seismic wavelength is longer than the size of the inhomogenities. A decrease in anisotropy and hence increase in scattering is observed with decreasing wavelength. A typical example of frequency-dependent scattering-induced anisotropy is the wave propagation in finely layered media (e.g. Shapiro *et al.* 1994; Werner & Shapiro 1999). Marson-Pidgeon

& Savage (1997) suggested aligned heterogeneities as the likely cause of FDA observations in teleseismic data.

The second proposed mechanism for FDA accounts for fluid flow in fractured porous rocks. Seismic waves propagating through fractured porous rocks can induce pressure gradients that cause fluid exchange between fractures and pore spaces to achieve pressure equalization (e.g. Chapman 2003). Thus, fluid-saturated fractured rocks are expected to show frequency-dependent velocity dispersion and attenuation, and hence FDA effect. Once again, there will be a decrease in percentage anisotropy with increasing frequency (e.g. Maultzsch *et al.* 2003; Al-Anboori *et al.* 2006).

Recent studies (e.g. Teanby *et al.* 2004a; Al-Harrasi *et al.* 2010) have shown the potential of using microseismic data to estimate reservoir seismic anisotropy via the use of SWS analysis. In this study, we report observations of frequency-dependent SWS made on microseismic data acquired from a petroleum field in Oman. First, we describe the study area and the data set. Then, we outline the theoretical modelling of FDA and we present some synthetic models and sensitivity analysis using the equivalent medium theory of Chapman (2003). After that, we describe the processing of the real data and the inversion of the FDA observations. The results are finally compared to those obtained from ordinary SWS analysis and outcrop observations.

2 STUDY AREA AND DATA SET

The field discussed in this study is located in Oman. It is in the form of a gently dipping anticline dome created by deep-seated salt movement (Litsey *et al.* 1986). The field formations are cut by two fault systems trending NE–SW and NW–SE, which are a consequence of regional tectonics (Fig. 1a). The NE–SW trending extensional faults form a central graben in the middle of the field.

The field consists of a chalky limestone formation overlain by shale cap rocks (Fig. 1b). The middle Cretaceous age carbonate formation comprises seven members: N–A (top) to N–G (bottom). Gas is produced by pressure depletion from the N–A reservoir. Production is highly dependent on fracture permeability. In this study, the non-producing part of the formation (N–B to N–G) is subdivided into: an upper part (N–1) and a lower part (N–2).

The microseismic data were acquired using five monitoring wells, each instrumented with 8-level seismic arrays (Fig. 1, Jones *et al.* 2004). Sensor orientation is well constrained for only 13 stations (denoted by black triangles in Fig. 1b), thus these are the only stations suitable for SWS and FDA analysis. Nearly 7500 events have been recorded over a period of 18 months (magnitude −2.5–0.5). The majority of the located events occurred within the compacting N–A reservoir and along the graben faults (Fig. 1).

Al-Harrasi *et al.* (2010) used the microseismic data set to estimate seismic anisotropy throughout the field using SWS analysis. The study revealed that the anisotropy is controlled by lithology and proximity to the graben faults. The percentage difference between the fast and slow shear wave velocities along the ray path (δV_s) is higher in the SE part of the field and the area between the graben faults (∼5 per cent), in comparison to the NW part (∼2 per cent). The highest amounts of δV_s (∼5 per cent) are within the highly fractured N–A reservoir. δV_s decreases with depth reaching about 1 per cent in the lowest parts of the N–2 unit. The shale exhibits moderate anisotropy with average δV_s of 4 per cent. The dip of the fractures is estimated to be subvertical. The fracture strike is variable, showing both NE–SW and NW–SE trends in most cases, consistent with known fault orientations (Fig. 1a).

3 THEORETICAL MODELLING OF FREQUENCY-DEPENDENT ANISOTROPY

Traditional equivalent medium theories for fractured media (e.g. Hudson 1981; Thomsen 1995) do not consider the frequency-dependence of elastic response. Such models lack the sensitivity to fracture size. For example, a medium with a few large fractures will generate elastic constants equivalent to those produced by a medium containing many small cracks. In recent years, several frequency-dependent models have been proposed which incorporate the effect of wave-induced fluid motion (Hudson *et al.* 1996; Pointer *et al.* 2000; van der Kolk *et al.* 2001). However, these model do not explain the frequency-dependance of seismic anisotropy for the entire frequency range appropriately, especially with the presence of fluid saturated fractures.

There have been some attempts in the past few years to model the FDA effects observed in real data. For example, Chesnokov *et al.* (2001) suggested a model of FDA in fractured media that accounts for seismic scattering due to ordered heterogeneities (ellipsoidal inclusions). It was used to model the FDA effect measured in the Bluebell-Altamont field VSP data. To explain the observed FDA effect, Chesnokov *et al.* (2001) assumed high concentration of large fractures (100 m in radius with aspect ratio of 0.06). Tod & Liu (2002) proposed a layer-bounded fracture model based on the equivalent medium theory of Hudson *et al.* (1996). The model describes the fluid flow between elliptical cracks (bed limited cracks in this case). It was used to simulate the FDA observations in earthquake data by Marson-Pidgeon & Savage (1997). In this study, we base our modelling on the poroelastic theory of Chapman (2003).

The poroelastic equivalent medium model of Chapman (2003) considers the case of a pore space which consists of a random isotropic collection of microcracks and spherical pores with aligned ellipsoidal fractures. It is an extension of the Chapman *et al.* (2002) model, which is restricted for squirt fluid flow within porous media (i.e. without fractures). The equant pores and microcracks in the Chapman (2003) model are on the scale of the grain size, whereas the aligned fractures are allowed to be much larger, as long as their size and spacing remain smaller than the seismic wavelength. Therefore, the model accounts for two different length scales and the resulting medium has hexagonal symmetry. The effective stiffness tensor can be expressed as

$$C_{ijkl} = C^{\circ}_{ijkl} - \Phi_p C^1_{ijkl} - \varepsilon C^2_{ijkl} - \xi C^3_{ijkl}, \quad (1)$$

where C° is the isotropic elastic tensor of the matrix and, C^1, C^2 and C^3 are the additional contributions from pores, microcracks and fractures, respectively, multiplied by the porosity (Φ_p), the crack density (ε) and the fracture density (ξ). In our case, C° is constructed using Lamé parameters λ and μ. The Chapman (2003) model is restricted to low porosity and valid for low concentrations of inclusions. Thus, for the cases of high porosity, the use of the grain moduli λ and μ to calculate the effect of fractures can result in substantial errors. Chapman *et al.* (2003b) proposed a modified version which overcomes the restriction to low porosity. They suggested using λ° and μ° which are derived from the velocities V_p° and V_s° of the unfractured porous rock. λ° and μ° are defined as

$$\mu^{\circ} = (V_s^{\circ})^2 \rho; \qquad \lambda^{\circ} = (V_p^{\circ})^2 \rho - 2\mu^{\circ}, \quad (2)$$

where ρ is the density of the saturated rock. Also, the isotropic tensor (C°) needs to be expressed in such away that the measured isotropic velocities are obtained by applying the pore and crack correction at a certain frequency $f_{\circ}$. The new Lamé parameters are

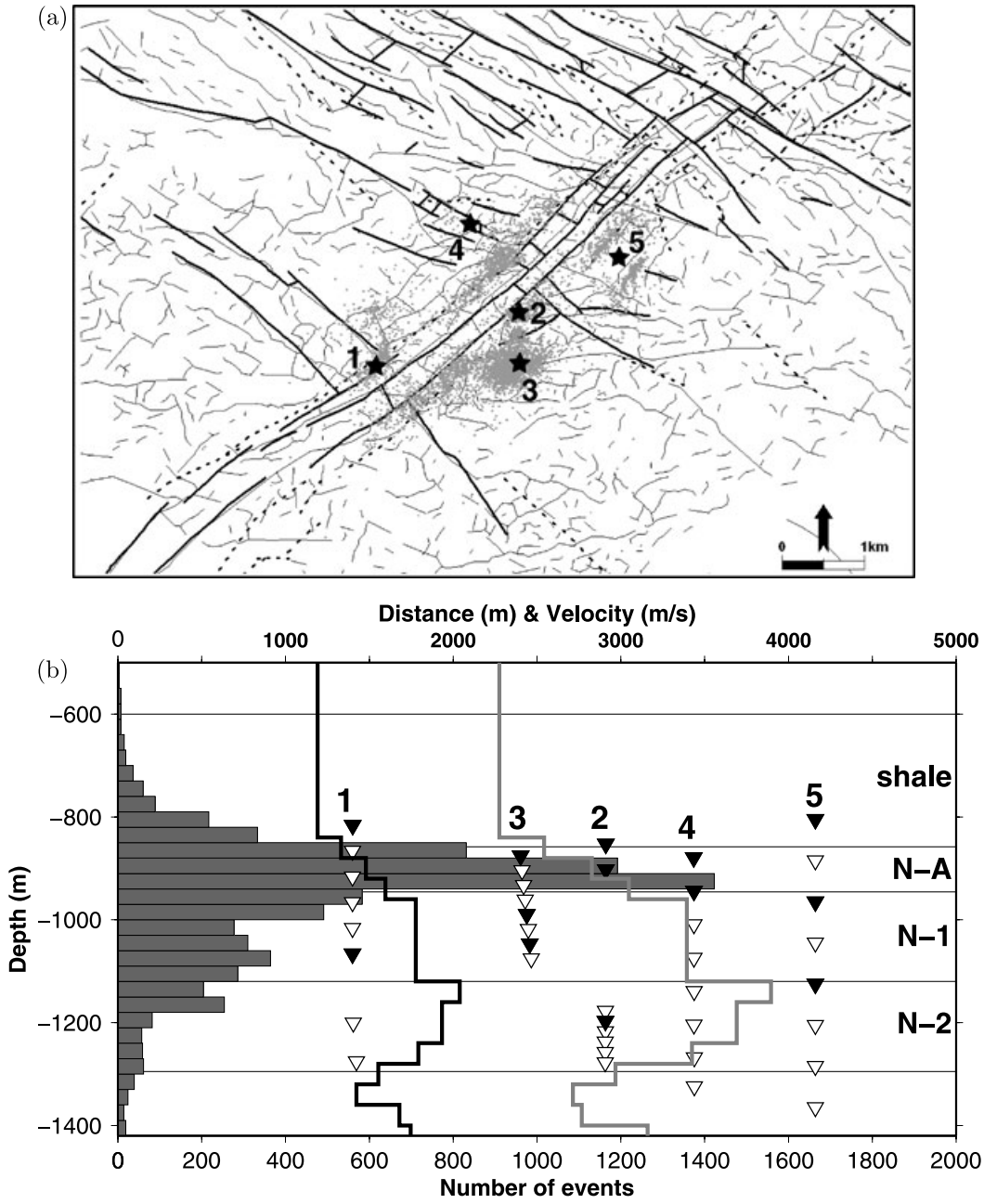

Figure 1. Microseismic monitoring in the field. (a) Major faults cutting the field formations at depths of ∼850 m (dashed line) and ∼1500 m (continuos line). Minor faults from 3-D survey are also shown by thin lines. Locations of the five monitoring wells are shown by black stars. The located microseismic events are marked by grey dots. (b) SW–NE oriented cross-section showing the microseismic network and histogram of the vertical distribution of seismicity. Seismic stations are marked by triangles and the ones with known sensor orientation are in black. The black and grey thick line show the 1-D *S*-wave and *P*-wave velocity models for the field, respectively.

defined as

$$\Upsilon = \mu^{\circ} + \Omega_{c,p}(\lambda^{\circ}, \mu^{\circ}, f_{\circ}); \qquad \Lambda = \lambda^{\circ} + \Omega_{c,p}(\lambda^{\circ}, \mu^{\circ}, f_{\circ}), \quad (3)$$

where $\Omega_{c,p}$ is perturbation function due to the presence of microcracks and pores. Now, $C^{\circ}(\Lambda, \Upsilon)$ is frequency independent and eq. (1) becomes

$$C_{ijkl}(f) = C^{\circ}_{ijkl}(\Lambda, \Upsilon) - \Phi_p C^1_{ijkl}(\lambda^{\circ}, \mu^{\circ}, f) - \varepsilon C^2_{ijkl}(\lambda^{\circ}, \mu^{\circ}, f) - \xi C^3_{ijkl}(\lambda^{\circ}, \mu^{\circ}, f), \quad (4)$$

where f is the frequency.

The Chapman (2003) model allows for fluid exchange between equant pore spaces and fractures. The model assumes that the pore spaces are fully saturated with one type of fluid. Chapman *et al.* (2003b) suggested that the model can be further simplified by ignoring ε for rocks with high Φ_p. Chapman *et al.* (2003b) argued that rocks with sufficient Φ_p can accommodate the expelled fluid from fractures. In contrast, for rocks with zero porosity, the expelled fluid is forced into the microcracks and the possibility for this to happen depends on ε. The porosity of the field rocks in this study is high (Table 1) and thus the microcrack effect can be ignored.

Table 1. Model input parameters used in the inversion. V_p and V_s are computed using the field 1-D velocity model (see Fig. 1b). Reference frequency ($f_\circ$) is 40 Hz. These parameters were delivered by the field operator.

Parameter	Shale	N–A	N–1	N–2
Density (kg m^{-3})	2200	2400	2400	2400
Porosity (per cent)	30	30	24	24
Permeability (mD)	1×10^{-4}	10	1	1
Viscosity (Pa s)	4.4×10^{-4}	1.42×10^{-5}	4.4×10^{-4}	4.4×10^{-4}
Relaxation time (s)	2.9	9.5×10^{-7}	2.9×10^{-4}	2.9×10^{-4}
Fluid type	Brine	Gas	Brine	Brine
Fluid bulk modulus (GPa)	2.3	0.0068	2.3	2.3
Fracture dip (° from horizontal)	72	73	73	63

The fluid flow in the model occurs at two scales: (1) the grain scale fluid flow described by the traditional squirt flow frequency [or relaxation time (τ_m)] and (2) the fracture scale fluid flow associated with larger timescale constant (τ_f). The two timescales are related by the expression

$$\tau_f = \frac{a_f}{\varsigma}\tau_m, \tag{5}$$

where a_f is the fracture radius (length of the major axis of a spheroid) and ς is the grain size. Eq. (5) demonstrates that τ_f is directly proportional to a_f. As fracture radius increases, the ratio of surface area to volume decreases, meaning more volume of fluid has to move through an element of surface area to equalise the induced pressure, which requires more time (Maultzsch *et al.* 2003).

The model is sensitive to fracture size and pore fluid type, and able to explain attenuation and velocity dispersion at seismic frequencies. It can be used to invert for fracture parameters using frequency-dependent shear wave anisotropy observations (e.g. Maultzsch *et al.* 2003; Al-Anboori *et al.* 2006) or *P*-wave attenuation (e.g. Maultzsch *et al.* 2007).

4 SYNTHETIC MODELLING

4.1 Model parameterization

The construction of the Chapman (2003) model requires predefining the following parameters: V_p and V_s velocities, the frequency at which velocities are estimated ($f_\circ$), saturated rock density (ρ), porosity (Φ_p), squirt flow relaxation time (τ_m), fluid bulk modulus (K_f) and fracture parameters [strike (α), dip (ϱ), density (ξ), radius (a_f) and aspect ratio]. Following the work of Maultzsch *et al.* (2003) and Al-Anboori *et al.* (2006) the aspect ratio of fractures is assumed to be very small (0.0001) so that the model is not sensitive to it. The ray azimuth and inclination are defined with respect to the fracture set strike (α) and dip (ϱ), respectively. Usually, the fracture density (ξ) and radius (a_f) are determined by inverting real data.

V_p and V_s are computed as average estimates along the ray path using the field velocity model (Fig. 1b). These velocities were measured at $f_\circ$=40 Hz (Al-Anboori 2006). Since we do not have independent estimates of τ_m for the field rocks, they have to be estimated from other published laboratory data. Calibration is performed following the fact that τ_m is proportional to viscosity (η) divided by permeability (κ) (e.g. Chapman *et al.* 2003a). For calibration, we use the $\tau_m = 20\,\mu s$ estimated by Chapman (2001) for a rock sample with η and κ of 7.5×10^{-3} Pa s and 250 mD, respectively. The τ_m calibration equation takes the form

$$\tau_m = \frac{2 \times 10^{-3}}{3}\left(\frac{\eta}{\kappa}\right). \tag{6}$$

Table 1 lists the input parameters for the shale, N–A, N–1 and N–2 formations. The cap rocks and the non-producing part of the carbonate formation are assumed to be brine saturated. The fracture parameters [strike (α), density (ξ) and radius (a_f)] are inverted for using the real data as described below in Section 6. The fracture strike (α) should be constrained in the model to limit the free parameters in the inversion to fracture density (ξ) and radius (a_f). However, we included it in the inversion because it is not well constrained from the observations of ordinary SWS (Al-Harrasi *et al.* 2010) due to the limited ray coverage in the vertical plane. The available observations show fractures oriented in multiple directions, reflecting the structural complexity of the field illustrated in Fig. 1a. These observations of variability in fracture orientation are supported by measurements from borehole techniques such as formation microimages. In contrast, the ray coverage in the horizontal plane is good, yielding better constrained estimates of fracture dip (ϱ), which we fix in the model (Table 1).

4.2 Model sensitivity

In this section, we use synthetic modelling to test the sensitivity of the Chapman (2003) model to each of the input parameters. The modelling also helps to visualize what we should expect to see in the real data. The N–A reservoir parameters summarized in Table 1 are used to carry out the tests. Based on the field velocity model, the average V_p and V_s velocities for the N–A reservoir are 2800 ms^{-1} and 1470 ms^{-1}, respectively. The aligned fracture set is assumed to have a_f of 1 m and ξ of 0.1, unless stated otherwise. We consider vertical fracture dip ($\varrho = 90^\circ$) with horizontal ray propagation. Horizontal ray propagation is assumed because the majority of the real data show subhorizontal ray propagation. The ray azimuth is 0° from north in all models. Note that varying α and ϱ is identical to varying ray azimuth and inclination, respectively. In the modelling, the percentage shear wave anisotropy (δV_s) is calculated using $(100 \times (S_p - S_q)/S_p)$, where S_p is the pure shear velocity and S_q is the quasi shear velocity.

The synthetic modelling reveals that the Chapman (2003) model of FDA is sensitive to α or ray azimuth, ϱ or ray inclination, a_f, ξ and τ_m (Fig. 2). The rest of the input parameters listed in Table 1 show no or minor sensitivity.

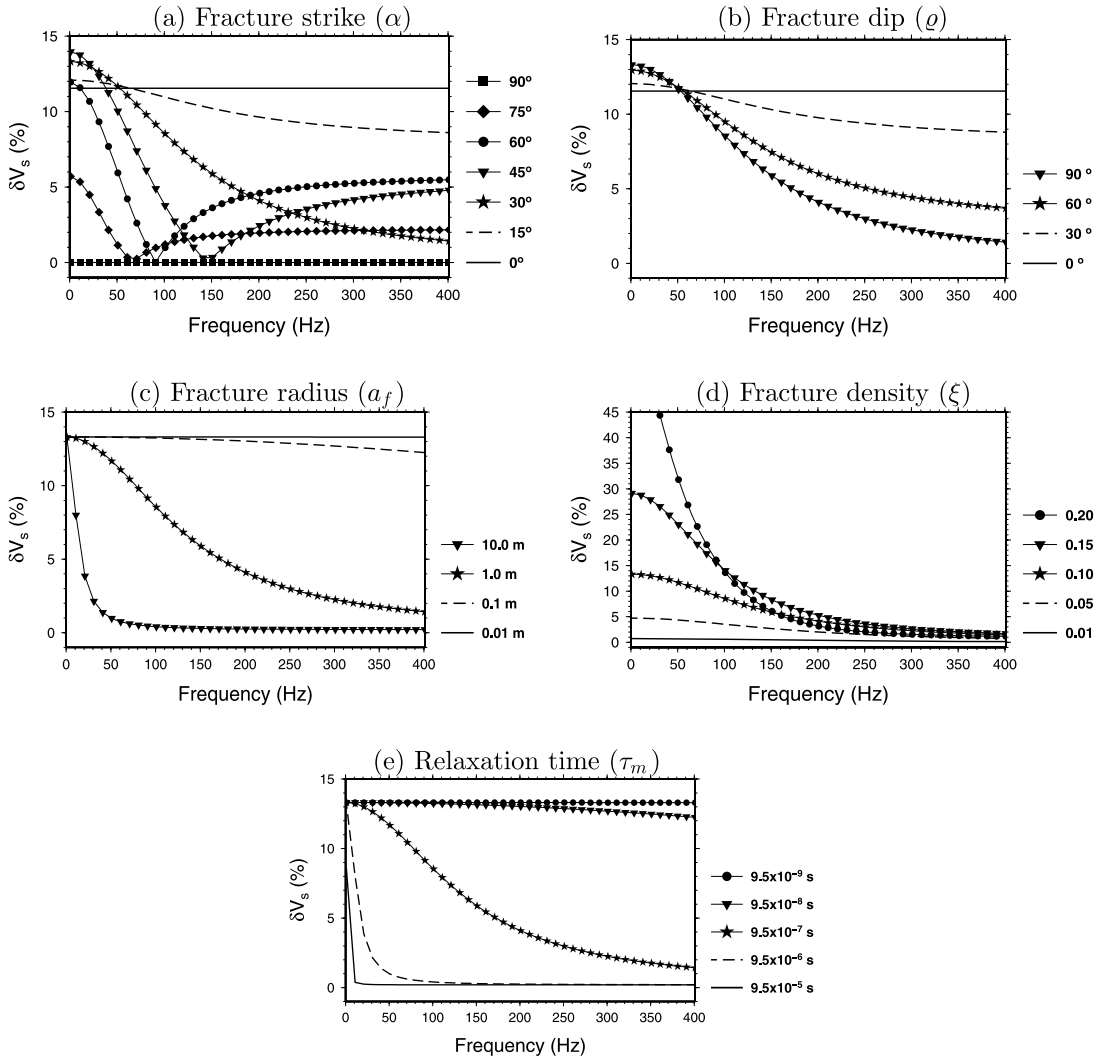

Figure 2. Synthetic modelling of frequency-dependent anisotropy. The models simulate the N–A reservoir (see Table 1). In (b), (c), (d) and (e), α is 30° from north. Fractures are dipping vertically (except in (b)) and the ray inclination is 90° from vertical.

4.2.1 Fracture strike (α)

As expected there is no splitting and thus there is no FDA effect for rays propagating perpendicular to the fracture plane (Fig. 2a). In contrast, SWS occurs when rays travel parallel to the fracture plane, but it is frequency-independent SWS. There are some cases where δV_s decays with increasing frequency until reaching zero and then starts increasing (cases of 45°, 60° and 75° in Fig. 2a). These are cases of crossing shear wave singularities, where the pure- and quasi shear waves have the same velocity. The pure shear wave has faster velocity than the quasi shear wave before the singularity point but after that the quasi shear wave is faster than the pure shear wave for higher frequencies. In the subsequent models, α is set to 30° as it shows a clear FDA effect without any singularity.

4.2.2 Fracture dip (ϱ)

There is no FDA effect when the fracture set is dipping horizontally (i.e. ray is travelling parallel to the fracture plane, Fig. 2b). The decay in δV_s gets sharper as the separation between the ray path and fracture plane increases. Note that fracture dip is measured from horizontal.

4.2.3 Fracture radius (a_f)

For fractures with large radii, there is a pronounced drop in δV_s at low frequencies (Fig. 2c). In contrast, the FDA effect is minor for the cases with small a_f and a drop in δV_s will occur at much higher frequencies.

4.2.4 Fracture density (ξ)

The magnitude of fracture density controls the sharpness of the drop in δV_s with increasing frequency (Fig. 2d). The FDA effect becomes more obvious with the increase in fracture density.

4.2.5 Relaxation time (τ_m)

Since τ_m and a_f are related by eq. (5), they show similar FDA responses (Figs 2c and e). The FDA effect is minor for small τ_m values. The model is very sensitive to τ_m and thus it has to be a highly accurate input to the model. Such accuracy can be obtained using measurements of frequency dispersion and attenuation using rock samples in laboratory experiments. Calibrating τ_m by extrapolating from one rock type to another, as we do in Section 4.1, can result

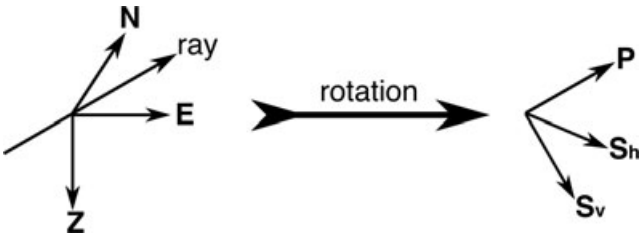

Figure 3. Rotation from the geographic east-north-vertical coordinates to the ray coordinates. After rotation, the *P*-wave component (P) is aligned along the ray direction. The horizontal *S*-wave component (S_h) is pointing horizontally and is perpendicular to the ray direction. The vertical *S*-wave component (S_v) is perpendicular to P and S_h components.

in significant and unquantifiable error. Such laboratory data are not available for the field rocks. Further suggestions for calibrating τ_m can be found in Maultzsch (2005) and Chapman *et al.* (2003a). For example, Maultzsch (2005) estimated τ_m by numerically fitting the Chapman (2003) model to the laboratory data of Rathore *et al.* (1995). This was done by modelling the velocity and attenuation measurements obtained by Rathore *et al.* (1995) for synthetic porous sandstone samples that were embedded with aligned fractures.

5 PROCESSING

Prior to the analysis, the data were filtered using a predictive filter to remove the 50 Hz electrical noise and its overtones. These are artefacts of electrical signals transmitted down the monitoring wells to prevent corrosion.

In the case of borehole monitoring, rays are not always at near-normal incidence, which means significant *S*-wave energy can be on the vertical component. Thus, the east, north and vertical seismograms are rotated into the ray coordinates using the polarization direction of the *P*-wave particle motion (Fig. 3). The rotation maximizes the *S*-wave arrival in the horizontal (S_h) and vertical (S_v) components, which are perpendicular to the ray direction component (P).

In the FDA analysis, we use events which have their ray paths entirely confined to each rock unit (i.e. shale cap rock, N–A reservoir, N–1 and N–2 units). Events with rays crossing the formation boundaries are excluded. Fig. 4 shows the *S*-wave frequency content for the microseismic data set for each formation. Generally, the shale cap rocks show narrower frequency bandwidths (10–200 Hz; Fig. 4a) compared to the carbonate rocks (10–400 Hz; Figs 4b–d), suggesting that shale is more attenuative than limestone.

The FDA analysis involves filtering the data into different frequency bands and estimating the splitting parameters (Φ and δt) for each passband. We follow the filtering methodology proposed by Al-Anboori *et al.* (2006). The filter has corner frequencies with a constant high to low frequency ratio of 2 (i.e. 1 octave). The frequency bands overlap as follows: 10–20 Hz, 15–30 Hz, 20–40 Hz, 30–60 Hz, etc. We use Butterworth bandpass filter with four poles and one pass. One pass filters are used to minimize ringing effects. This should not affect the estimate of δt because we seek relative time rather than absolute time. Furthermore, the dominant *S*-wave frequency (f_d) for each frequency band is calculated following the definition of Barnes (1993)

$$f_d^2 = \frac{\int_0^\infty f^2 P(f) df}{\int_0^\infty P(f) df}, \tag{7}$$

where f is the frequency and $P(f)$ is the power spectrum.

We use the automated SWS splitting approach of Wüstefeld *et al.* (2010) to estimate the splitting parameters. The approach is based on the SWS cluster analysis technique of Teanby *et al.* (2004b) and the null detection method of Wüstefeld & Bokelmann (2007). It combines the use of the cross-correlation method (e.g. Fukao 1984; Bowman & Ando 1987) and the eigenvalue minimization method (e.g. Silver & Chan 1988, 1991). The cross-correlation method derives the splitting parameters by rotating and cross-correlating the *S*-wave components in the *S*-wave plane to find the orientation with the highest cross-correlation coefficient. In contrast, the eigenvalue minimization method finds the splitting parameters by linearizing the *S*-wave particle motion, thereby removing the effects of the anisotropy. A grid search over $0 < \delta t \leq 40$ ms and $-90^\circ \leq \Phi \leq 90^\circ$ is used to find which best combination of Φ and δt that removes the anisotropy effect (i.e. linearize the *S*-wave elliptical particle motion). However, with narrow frequency bands, SWS analysis is often prone to cycle skipping (Teanby *et al.* 2004b). This leads to fluctuation in Φ, even for events which show systematic decrease in δt with increasing frequency. The Chapman (2003) model predicts a decay in δt, but a constant Φ. Therefore, we fix Φ, *a priori*, to the value determined using the SWS analysis on the broad-band data. δt is then estimated while searching over a narrow range of $\pm\ 10^\circ$ from Φ. The $\pm\ 10^\circ$ range accounts for the maximum acceptable error on Φ when analysing the broad-band data (Al-Harrasi *et al.* 2010). The main advantage of Wüstefeld *et al.* (2010) approach is that it provides an automated measure of the splitting reliability by comparing the splitting parameters from the cross-correlation and the eigenvalue minimization methods. In this way, we minimize human interaction and hence remove the subjectivity when assessing the reliability of the SWS measurements.

It is worth mentioning that Φ can also show dependence on frequency (e.g. Liu *et al.* 2006; Rumpker *et al.* 1999). Liu *et al.* (2006) observed different Φ for different frequencies in the presence of multiple fracture sets with different orientation and size. In such cases, low frequencies will sense large fractures whereas high frequencies will sense small ones. However, in our study the good FDA measurements do not show appreciable variation in Φ with increasing frequency. Therefore, we fix the search over Φ to be within $\pm\ 10^\circ$ of the value determined by the SWS analysis of the broad-band data.

The percentage difference between the fast and slow shear wave velocities along the ray path (δV_s) is computed using $(100 \times V_{s_{avg}} \times \delta t / D)$, where D is the straight line source–receiver ray path and $V_{s_{avg}}$ is the average *S*-wave velocity along D based on the 1-D velocity model of the field (Fig. 1b). The estimates of δV_s and shear wave dominant frequencies (f_d) are then used to invert for the fracture parameters.

6 INVERSION

We invert for the fracture strike (α), fracture density (ξ) and fracture radius (a_f) that best matches the observations of FDA using the poroelastic model of Chapman (2003). A grid search is performed over the three fracture parameters to find the best combination that minimizes the RMS misfit between the real and modelled data. It is performed in two steps. During the first step, while varying α with fixed steps of 5°, a_f and ξ are varied in power steps of 10^n to find in what order of magnitudes they fall. The second step is to search in finer detail around the a_f and ξ values obtained in the first step. This allows searching over a wide range of possible fracture parameters in a fast and convenient way and without any prior knowledge of the

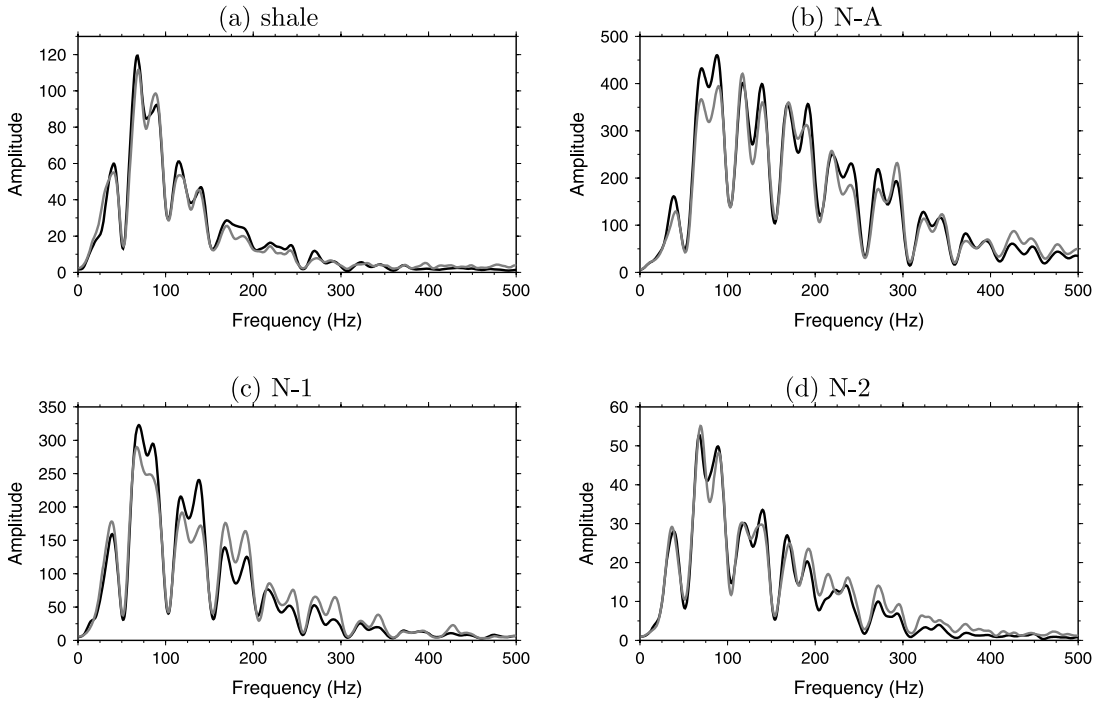

Figure 4. Frequency content of the *S*-wave arrivals within the (a) shale cap rocks, (b) N-A gas reservoir, (c) N-1 carbonate unit and (d) N-2 carbonate unit. Frequency spectrum is plotted for the horizontal (black) and vertical (grey) *S*-wave components (see Fig. 3).

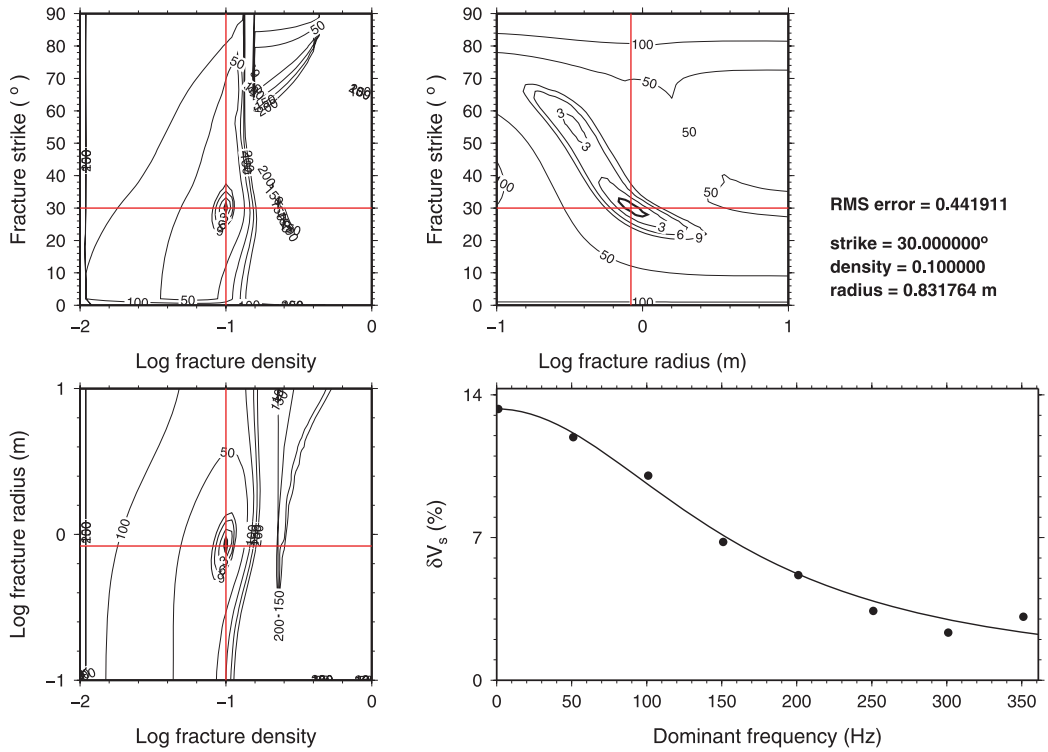

Figure 5. Inversion of frequency-dependent anisotropy synthetic data. Grid searches over fracture strike, density and radius. The thick black contour is the 90 per cent confidence interval. The straight red lines in the error plots mark the optimum fracture parameters. The right-bottom plot depicts the input synthetic data (dots) and the best-fit model (line). Random noise has been added to the synthetic data.

Table 2. Summary of fracture parameters obtained from frequency-dependent anisotropy inversion. Note that strike has 90° ambiguity. Numbers between brackets are average estimates.

Formation	Number of observations	Strike	Density	Radius (m)
Shale	4	variable	0.11–0.28 (0.18)	3×10^{-7} to 2×10^{-6} (1.3×10^{-6})
N–A	11	NE or NW	0.063–0.16 (0.11)	0.1–9.1 (2.5)
N–1	9	variable	0.036–0.21 (0.10)	0.005–0.04 (0.012)
N–2	2	variable	0.076–0.083 (0.08)	0.013–0.02 (0.017)

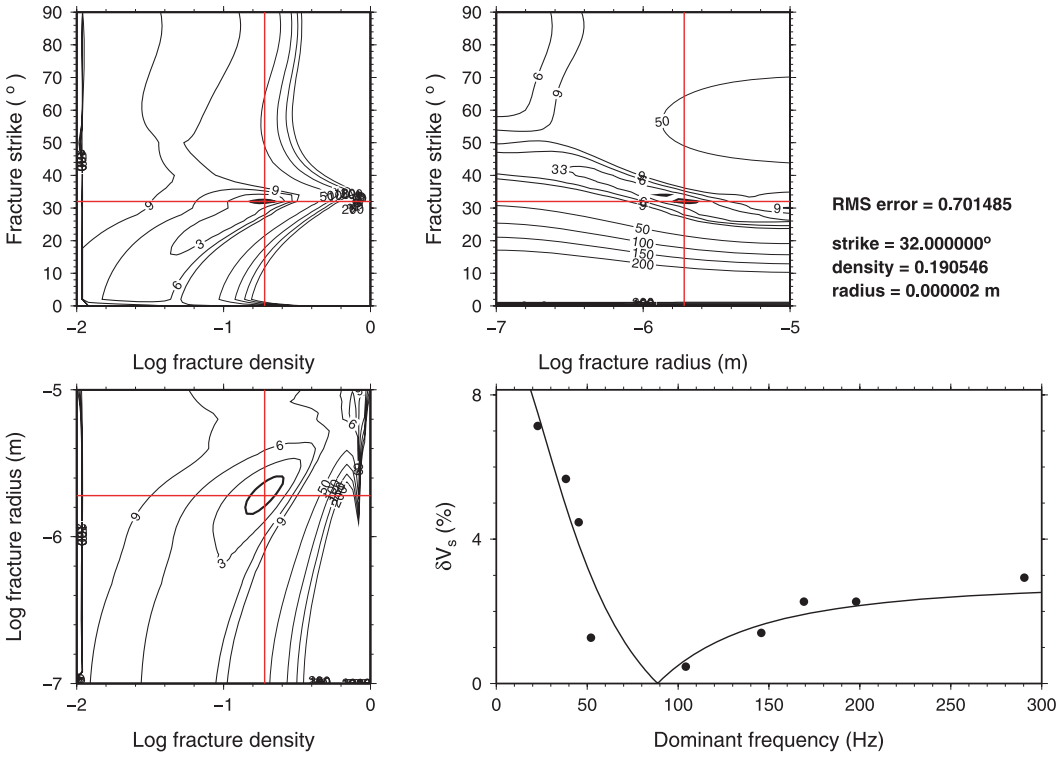

Figure 6. An example of frequency-dependent anisotropy inversion in the shale cap rocks. Grid searches over fracture strike, density and radius. The thick black contour is the 90 per cent confidence interval. The straight red lines in the error plots mark the optimum fracture parameters. The right-bottom plot depicts the real data (dots) and the best-fit model (line). Note the singularity point (i.e. δV_s=0 per cent) at frequency ∼90 Hz.

expected parameters. For example, the code searches for all possible values of a_f from the microscale (10^{-6}) up to hundreds of metres. Note that the grid search over α suffers a 90° ambiguity (e.g. α of 45° and 135° generate identical FDA effect). Thus, the grid search over α is restricted to the range $0 \leq \alpha \leq 90°$.

The confidence in the results is assessed using an F-test (e.g. Silver & Chan 1991). The 90 per cent confidence interval is computed by normalizing the RMS misfit surfaces. Also, the optimum fracture parameters from the inversion are used to generate the best fit model, which is then plotted with the real data to illustrate the match between them. Visual inspection of the plots is used to choose measurements with well constrained solutions.

To examine the robustness of the inversion, we generated synthetic models using the N–A reservoir parameters summarized in Table 1, with a vertically dipping fracture set having density of 0.1 and radius of 1 m. The fracture strike, ray azimuth and ray inclination are set to 30° from north, 0° from north and 90° from vertical, respectively. Noise is added to the calculated δV_s using random distribution of δV_s magnitudes in the range 0–2 per cent. The modelled data are then fed to the inversion code. The results are illustrated in Fig. 5. It can be seen that the inversion is very robust and it gives estimates ($\alpha = 30°$, $\xi = 0.1$ and $a_f = 0.83$) which are very close to the original inputs, despite the addition of noise.

7 RESULTS

We analyse events that have their ray paths entirely confined to the lithology units. FDA effect has been observed in 11 events within the shale cap rocks, 46 events within the N–A gas reservoir, 24 events within the N–1 unit and 6 events within the N–2 unit. The number of FDA observations which passed the visual inspection after the inversion is four for the shale cap rocks, 11 for the N–A reservoir, nine for the N–1 unit and two for the N–2 unit. The results from the inversion are summarized in Table 2. Examples of good inversions from each of the investigated lithology units are displayed in Figs 6–9.

The results from the inversion suggest that anisotropy is caused by microscale cracks in the shale cap rocks (1.3×10^{-6} m), metre-scale fractures in the N–A reservoir (2.5 m) and centimetre-scale fractures in the N–1 (0.012 m) and N–2 (0.017 m) units. There is a general decline in fracture density with depth. The average fracture density decreases from 0.18 within the shale cap rocks, to 0.11

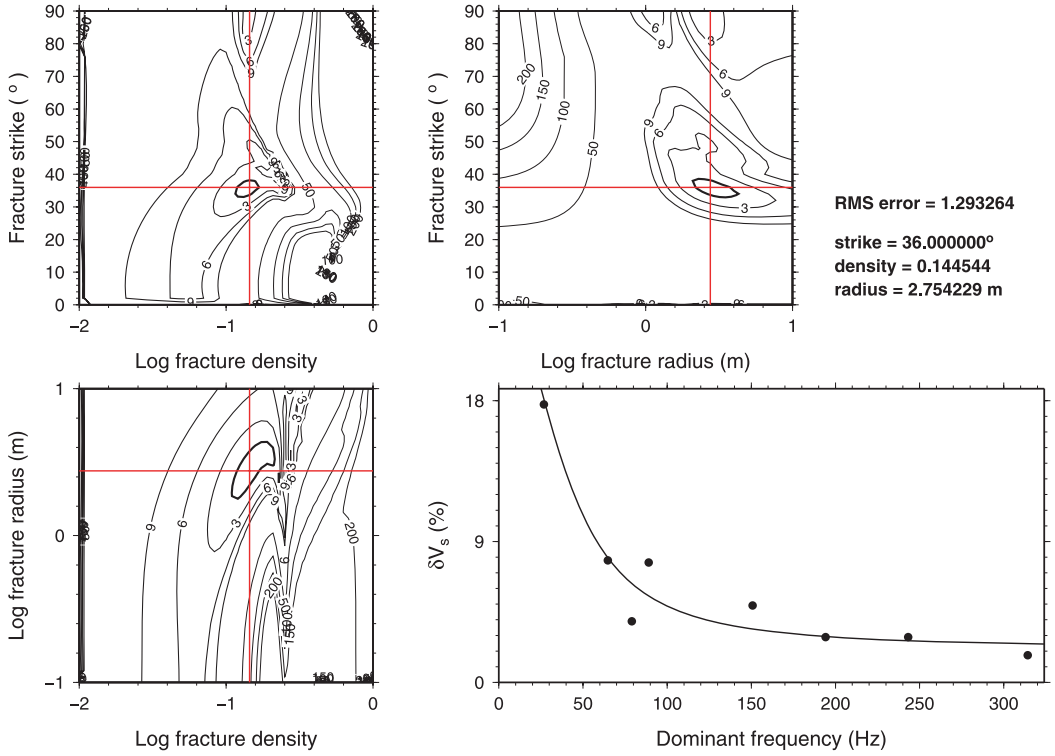

Figure 7. An example of frequency-dependent anisotropy inversion in the N–A reservoir (see caption of Fig. 6).

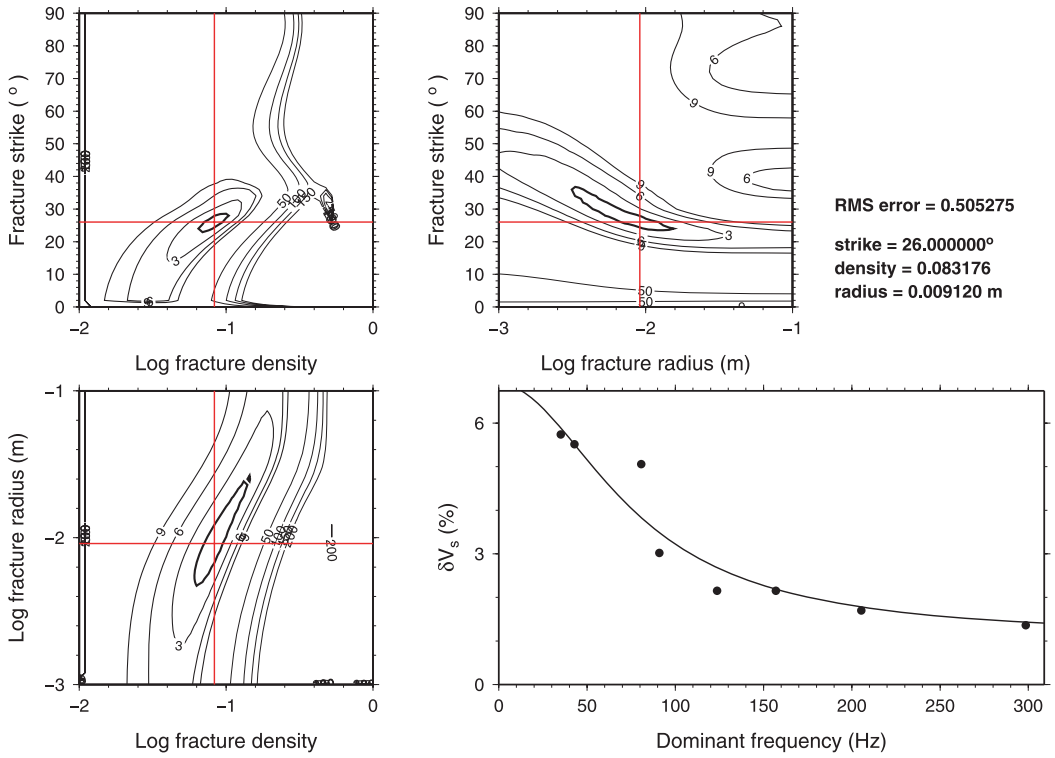

Figure 8. An example of frequency-dependent anisotropy inversion in the N–1 unit (see caption of Fig. 6).

within the N–A reservoir, to 0.10 within the N–1 unit, to 0.08 within the N–2 unit. Further investigation of fracture density, summarized in Table 3 and illustrated in Fig. 10, reveals that fracture density is also varying laterally between the field blocks (SE, Graben and NW) which are separated by the major graben faults. There is a gradual decrease in fracture density in the NW direction, crossing the main graben faults. When considering the entire data set, fracture density decreases from 0.13 in the SE block to 0.081 in the Graben block

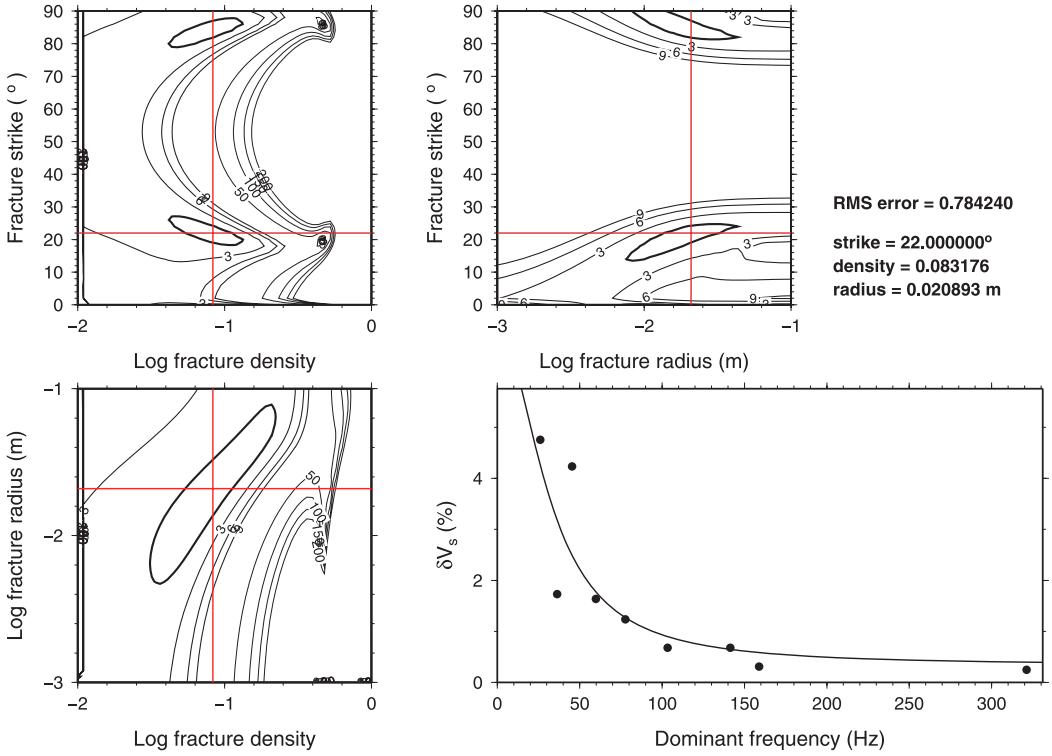

Figure 9. An example of frequency-dependent anisotropy inversion in the N–2 unit (see caption of Fig. 6).

Table 3. Variation of fracture density between field blocks. These are average estimates with the number between the brackets indicating the number of measurements.

Data set	SE block	Graben block	NW block
All	0.13 (18)	0.081 (3)	0.075 (5)
Shale	0.18 (4)	-	-
N–A	0.11 (9)	-	0.085 (2)
N–1	0.11 (5)	0.083 (1)	0.067 (3)
N–2	-	0.08 (2)	-

to 0.075 in the NW block. The results of fracture strike show wide variability (Table 2) and they possess 90° ambiguity. Thus, we avoid using them in the subsequent interpretation.

8 DISCUSSION

There is a good match between the real and modelled data, and the inversion for fracture parameters is robust. Furthermore, the consistency in the estimates of fracture density and size within each of the investigated lithology units (Table 2) indicates the reliability of the inversion. However, there is some uncertainty in our results due to a lack of knowledge of the relaxation time (τ_m). An estimate of fracture radius (a_f) is highly dependent on τ_m, as highlighted by eq. (5). Since, we do not have measurements of τ_m for the field rocks, we estimate τ_m using published laboratory data. However, extrapolating from one rock type to another may result in significant and unquantifiable error which is then mapped into the fracture parameters obtained through inversion.

There is no independent estimate of fracture size within the field to compare with. Al-Kindi (2006) analysed data from the N–A formation outcrops. The exposed formation contains fractures with lengths in the range 4–22 m and aperture between 3 and 14 mm.

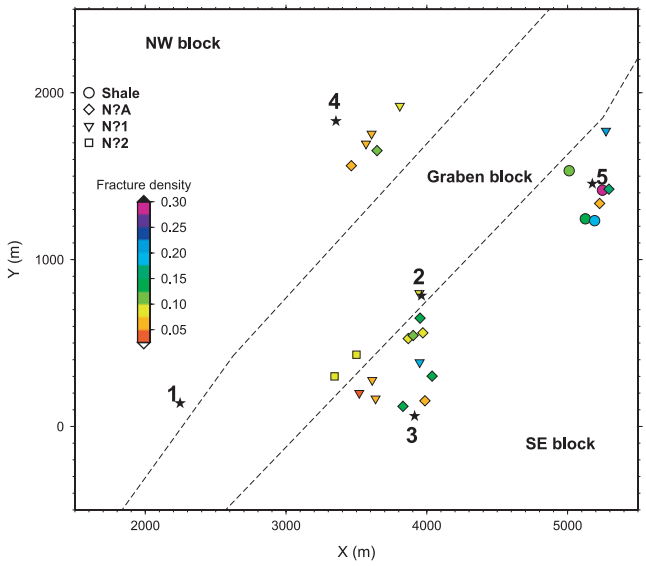

Figure 10. Lateral variation in fracture density. Measurements are plotted at source–receiver midpoints. The average fracture density decreases from 0.13 in the SE block to 0.081 in the Graben block to 0.075 in the NW block. The major graben faults are shown by dashed lines. The five monitoring wells are marked by stars.

Fracture aperture is expected to be much smaller in the subsurface due to the burial effect. Note that the FDA inversion provides the fracture radius (length of major axis of spheroid) rather than the length. So the modelled N–A fracture size and that observed in the outcrops are in the same order of magnitude. The microscale fracture size shown by the shale data set indicates that macroscale fractures are absent in the cap rock and the fluid communication, causing the FDA effect, occurs between pores and microscale

cracks. This highlights the potential importance of the FDA analysis for assessing seal integrity.

There is a general decrease in fracture density with depth. The average fracture density decreases from 0.18 in the shale cap rocks to 0.11 in the N–A reservoir to 0.1 in the N–1 unit to 0.08 in the N–2 unit. This decrease in fracture density is consistent with the magnitudes of δV_s estimated by Al-Harrasi *et al.* (2010), that the shale and N–A reservoir exhibit higher magnitudes of anisotropy compared to the underlying N–1 and N–2 formations. Furthermore, the lateral decrease in average fracture density from 0.13 in the SE block to 0.081 in the Graben block to 0.075 in the NW block matches with the observations that the highest amounts of anisotropy lie to the SE part of the field and between the graben faults.

Our observations of FDA also helps calibrate other independent observations of seismic anisotropy. For example, azimuthal variations in amplitudes (e.g. Hall & Kendall 2003) and converted wave properties (e.g. Thomsen 1999) are considered as evidences of anisotropy, but the length-scale of the causative mechanism is unknown. FDA analysis of microseismic data would help with the interpretation of these other anisotropy techniques.

9 CONCLUSION

We have investigated observations of frequency-dependent shear wave splitting anisotropy made on microseismic data from a gas field. The poroelastic model of Chapman (2003) is used to model the observations and invert for fracture orientation, density and size.

The estimated fracture sizes within the N–A gas reservoir agree with those observed in the formation outcrops. The variation in fracture density with lithology matches with the estimates of anisotropy magnitudes deduced from ordinary SWS analysis. Higher magnitudes of fracture density and anisotropy occur within the shale and N–A gas reservoir compared to the underlying non-producing N–1 and N–2 carbonate units.

Cumulatively, the results show that the modelling of the frequency-dependent behaviour of anisotropy based on squirt fluid flow mechanism serves as a tool to characterize reservoirs and assess seal integrity. However, there may be other mechanism (e.g. scattering) which can cause FDA effect that future work will explore them.

ACKNOWLEDGMENTS

We thank the Ministry of Oil and Gas (Sultanate of Oman) and Petroleum Development Oman (PDO) for their permission to publish the results. Othman Al-Harrasi was funded by a PDO scholarship. We also like to thank the *GJI* associate editor Jeannot Trampert, and reviewers Enru Liu and Martha Savage for their constructive comments which have improved the manuscript substantially.

REFERENCES

Al-Anboori, A., 2006. Anisotropy, focal mechanisms and state of stress in an oilfield: passive seismic monitoring in Oman, *PhD thesis*, University of Leeds.

Al-Anboori, A., Kendall, J.-M., & Chapman, M., 2006. Fracture-induced frequency-dependent anisotropy, Yibal Field, Oman, *Proc. EAGE 68th Conference and Technical Exhibition,* Expanded Abstracts, Vienna, Austria, A047.

Al-Harrasi, O., Al-Anboori, A., Wüstefeld, A. & Kendall, J.-M., 2010. Seismic anisotropy in a hydrocarbon field estimated from microseismic data, *Geophys. Prospect.,* **59**(2), 227–243.

Al-Kindi, M., 2006. Structural evolution and fracture pattern of Salakh arch, *PhD thesis*, University of Leeds.

Barnes, A.E., 1993. Instantaneous spectral bandwidth and dominant frequency with applications to seismic reflection data, *Geophysics,* **58**(3), 419–428.

Bowman, J.R. & Ando, M., 1987. Shear-wave splitting in the upper-mantle wedge above the Tonga subduction zone, *Geophys. J. R. astr. Soc.,* **88**(1), 25–41.

Carter, A.J. & Kendall, J.-M., 2006. Attenuation anisotropy and the relative frequency content of split shear waves, *Geophys. J. Int.,* **165**(3), 865–874.

Chapman, M., 2001. Modelling the wide-band laboratory response of rock samples to fluid pressure changes, *PhD thesis*, University of Edinburgh.

Chapman, M., 2003. Frequency-dependent anisotropy due to meso-scale fractures in the presence of equant porosity, *Geophys. Prospect.,* **51**(5), 369–379.

Chapman, M., Zatsepin, S. & Crampin, S., 2002. Derivation of a microstructural poroelastic model, *Geophys. J. Int.,* **151**(2), 427–451.

Chapman, M., Maultzsch, S. & Liu, E., 2003a. Some estimates of the squirt-flow frequency, *SEG Annual Meeting,* Dallas, TX.

Chapman, M., Maultzsch, S., Liu, E. & Li, X., 2003b. The effect of fluid saturation in an anisotropic multi-scale equant porosity model, *J. appl. Geophys.,* **54**(3-4), 191–202.

Chesnokov, E., Queen, J., Vichorev, A., Lynn, H., Hooper, J., Bayuk, I., Castagna, J. & Roy, B., 2001. Frequency dependent anisotropy, in *SEG Expanded Abstracts,* Vol. 20(1), pp. 2120–2123.

Fukao, Y., 1984. Evidence from core-reflected shear waves for anisotropy in the Earth's mantle, *Nature,* **309**(5970), 695–698.

Hall, S.A. & Kendall, J.-M., 2003. Fracture characterization at Valhall: application of P-wave amplitude variation with offset and azimuth (AVOA) analysis to a 3D ocean-bottom data set, *Geophysics,* **68**(4), 1150–1160.

Hudson, J.A., 1981. Wave speeds and attenuation of elastic waves in material containing cracks, *Geophys. J. R. astr. Soc.,* **64**(1), 133–150.

Hudson, J.A., Liu, E. & Crampin, S., 1996. The mechanical properties of materials with interconnected cracks and pores, *Geophys. J. Int.,* **124**(1), 105–112.

Jones, R.H., Raymer, D., Mueller, G., Rynja, H. & Maron, K., 2004. Microseismic monitoring of the Yibal Oilfield, in *EAGE 66th Conference and Exhibition,* Expanded Abstracts, A007, Paris, France.

van der Kolk, C.M., Guest, W.S. & Potters, J.H.H.M., 2001. The 3D shear experiment over the Natih field in Oman: the effect of fracture-filling fluids on shear propagation, *Geophys. Prospect.,* **49**(2), 179–197.

Litsey, L.R., MacBride, W.L., Al-Hinai, K.M. & Dismukes, N.B., 1986. Shuaiba reservoir geological study, Yibal Field, Oman, *J. Petrol. Tech.,* **38**(7), 651–661.

Liu, E., Queen, J.H., Li, X.Y., Chapman, M., Maultzsch, S., Lynn, H.B. & Chesnokov, E.M., 2003. Observation and analysis of frequency-dependent anisotropy from a multicomponent VSP at Bluebell-Altamont field, Utah, *J. appl. Geophys.,* **54**(3-4), 319–333.

Liu, E., Chapman, M., Zhang, Z. & Queen, J.H., 2006. Frequency-dependent anisotropy: effects of multiple fracture sets on shear-wave polarizations, *Wave Motion,* **44**, 44–57.

Marson-Pidgeon, K. & Savage, M.K., 1997. Frequency-dependent anisotropy in Wellington, New Zealand, *Geophys. Res. Lett.,* **24**(24), 3297–3300.

Maultzsch, S., 2005. Analysis of frequency-dependent anisotropy in VSP data, *PhD thesis*, University of Edinburgh.

Maultzsch, S., Chapman, M., Liu, E. & Li, X., 2003. Modelling frequency-dependent seismic anisotropy in fluid-saturated rock with aligned fractures: implication of fracture size estimation from anisotropic measurements, *Geophys. Prospect.,* **51**(5), 381–392.

Maultzsch, S., Chapman, M., Liu, E. & Li, X., 2007. Modelling and analysis of attenuation anisotropy in multi-azimuth VSP data from the Clair field, *Geophys. Prospect.,* **55**(5), 627–642.

Pointer, T., Liu, E. & Hudson, J.A., 2000. Seismic wave propagation in cracked porous media, *Geophys. J. Int.,* **142**(1), 199–231.

Rathore, J., Fjaer, E., Holt, R. & Renlie, L., 1995. P-wave and S-wave anisotropy of a synthetic sandstone with controlled crack geometry, *Geophys. Prospect.,* **43**(6), 711–728.

Rumpker, G., Tommasi, A. & Kendall, J.M., 1999. Numerical simulations of depth-dependent anisotropy and frequency-dependent wave propagation effects, *J. Geophys. Res.-Solid Earth,* **104**(B10), 23 141–23 153.

Shapiro, S.A., Zien, H. & Hubral, P., 1994. A generalized ODoherty-Anstey formula for waves in finely layered media, *Geophysics,* **59**(11), 1750–1762.

Silver, P.G. & Chan, W.W., 1988. Implications for continental structure and evolution from seismic anisotropy, *Nature,* **335**(6185), 34–39.

Silver, P.G. & Chan, W.W., 1991. Shear wave splitting and subcontinental mantle deformation, *J. geophys. Res.,* **96**(B10), 16429–16454.

Teanby, N., Kendall, J.-M., Jones, R.H. & Barkved, O., 2004a. Stress-induced temporal variations in seismic anisotropy observed in microseismic data, *Geophys. J. Int.,* **156**(3), 459–466.

Teanby, N., Kendall, J.-M. & van der Baan, M., 2004b. Automation of shear-wave splitting measurements using cluster analysis, *Bull. seism. Soc. Am.,* **94**(2), 453–463.

Thomsen, L., 1995. Elastic anisotropy due to aligned cracks in porous rock, *Geophys. Prospect.,* **43**(3), 805–829.

Thomsen, L., 1999. Converted-wave reflection seismology over inhomogeneous, anisotropic media, *Geophysics,* **64**(3), 678–690.

Tod, S. & Liu, E., 2002. Frequency-dependent anisotropy due to fluid flow in bed limited cracks, *Geophys. Res. Lett.,* **29**(15), 39–41.

Werner, U. & Shapiro, S., 1999. Frequency-dependent shear-wave splitting in thinly layered media with intrinsic anisotropy, *Geophysics,* **64**(2), 604–608.

Wüstefeld, A. & Bokelmann, G., 2007. Null detection in shear-wave splitting measurements, *Bull. seism. Soc. Am.,* **97**(4), 1204–1211.

Wüstefeld, A., Al-Harrasi, O.H., Verdon, J.P., Wookey, J. & Kendall, J.M., 2010. A strategy for automated analysis of passive microseismic data to study seismic anisotropy and fracture characteristics, *Geophys. Prospect.,* **58**, 755–773.